Effects of Pressure and Electric Field Strength on the Emission Rate for a Molecular Dynamics Model of [EMIM][BF$_4$] Ionic Liquid

Tanapat Bhakyapaibul[1], Avinash Rao[2], Deborah Levin[3], Huck Beng Chew[4], and Joshua L. Rovey[5]

University of Illinois Urbana-Champaign, Urbana, IL, 61801, USA

Through an all-atom molecular dynamics approach, a model of a bulk ionic liquid in the presence of an applied electric field is developed to study the relationship between the pressure associated with a mass flow through an emitter, the applied electric field strength, and the resulting ion emission rates for 1-Ethyl-3-methylimidazolium tetrafluoroborate ([EMIM][BF$_4$]). In these simulations, a force is applied to a rigid wall located below the bulk ionic liquid placed in a domain that is laterally periodic and fixed in the Z-direction. A nanopore placed above the bulk ionic liquid allows molecules to form a convex meniscus due to the intrinsic surface tension of the ionic liquid. When an electric field is applied to the ionic liquid, ion emissions are produced from the meniscus as long as the force on the liquid due to the field is able to overcome the surface tension of the [EMIM][BF$_4$] . As a pressure differential is applied and the electric field strength is varied, the emission rate changes, and a relationship is developed for the adjustable parameters and the resulting flow of ions. Experimental work on secondary mass flux was carried out in conjunction with the simulations. A diagnostic for measuring ejected mass at a polar angle from a bombarded target was developed and measurements were made to validate the methodology and characterize the energy dependence and angular profile. Mass flux yields from a high voltage primary plume dropped from 7.304×10^{-14} $\frac{ng}{ion\text{-}sr}$ at a polar angle of $35°$ to 3.645×10^{-14} $\frac{ng}{ion\text{-}sr}$ at $80°$. When spraying a low voltage plume, the yields were relatively constant across the set of polar angles, with values ranging from 7.391×10^{-14} $\frac{ng}{ion\text{-}sr}$ to 8.828×10^{-14} $\frac{ng}{ion\text{-}sr}$. Results indicate that the high energy plume produces a secondary plume with less mass than atomic carbon sputtering nickel, but more mass than if the carbon atoms simply bounced off the surface of the target.

[1]Graduate Research Assistant, Department of Aerospace Engineering, tanapat2@illinois.edu
[2]Graduate Research Assistant, Department of Aerospace Engineering, avinash4@illinois.edu
[3]Professor, Department of Aerospace Engineering, and AIAA Fellow, deblevin@illinois.edu
[4]Associate Professor, Department of Aerospace Engineering, hbchew@illinois.edu
[5]Professor, Department of Aerospace Engineering, and AIAA Associate Fellow, rovey@illinois.edu

1

I. Nomenclature

a = polar angle [°]

A_S = QCM crystal electrode surface area $\left[\text{cm}^2\right]$

b_z = length perpendicular to liquid-vacuum interface used for pressure scaling

C = mass sensitivity constant $\left[\frac{\text{ng}}{\text{Hz}-\text{cm}^2}\right]$

$\frac{dm}{dt}$ = mass deposition rate [ng/s]

J_T = Plume current [A]

n = thin film overtone number

ΔP = pressure differential across meniscus surface

q = charge on ion [C]

γ = surface tension

P_{ij} = ij-component of pressure with i = j = x, y, or z

R = principal radius of curvature

r = separation between surface and QCM [cm]

R = principal radius of curvature

R_1 = principal radius of curvature in XZ-plane

R_2 = principal radius of curvature in YZ-plane

II. Introduction

Ionic liquids are neutrally charged salts known for their stability as liquids under a variety of pressure and temperature conditions. These liquids emit ions when exposed to electric fields and are used as a source of propulsion in electrospray thrusters. In order to produce a steady flow of emissions, the force of the applied electric field must overcome the intrinsic surface tension of the ionic liquid. Modeling the surface tension is crucial to capturing the relationship between the pressure difference across the ionic liquid meniscus, the applied electric field, and the resulting emission rate. This allows for the prediction of the critical field strength and pressure where a convex meniscus may transition to a Taylor Cone and produce steady emissions. In these electrospray systems, the ionic liquid is fed through an emitter at a specified mass flow rate which is associated with a force on the bulk ionic liquid. This force produces a resulting pressure differential at the liquid-vacuum interface and leads to the formation of a convex meniscus. Developing a molecular dynamics model of these systems at the atomic scale makes it possible to determine the species emitted from a bulk ionic liquid in the presence of an electric field that may not be resolved at larger scales. Predicting the conditions necessary to produce steady ion emission rates and the ability to determine the species emitted will enable the design of propulsion systems that can prioritize thrust or specific impulse which are both dependent on the emission mode. While molecular dynamics is limited to atomic time- and length-scales, the results from these simulations can be used to inform larger-scale models that more accurately reflect experimental setups. These results will allow for the characterization of the primary emissions that may fragment to form secondary emissions that leave behind neutrals that could be deposited on and erode a thruster surface.

Models like the one detailed in this study are essential for predicting key performance parameters, and they rely on empirical data to enhance the accuracy of their results. As a result, the results from terrestrial facilities must be entirely understood and assessed with proper context and compensation for the effects of the interactions between the thruster and its test environment. Given that a majority of electrospray diagnostics involve directly receiving the plume of charged species on electrical measurement devices or pressure sensors, the interactions between the plume species and the experimental surfaces must be taken into account. Facility effects have been and continue to be thoroughly studied for existing and proven EP technologies like Hall thrusters due to their sensitivity to background pressure and the impacts of electrical coupling on the thruster plasma. Conversely, electrospray facility effects have only recently come under intense scrutiny from the community.

Beyond the effects of ground-based testing, EP systems may pose a threat to their spacecraft if their interactions with other subsystems are not fully considered. Of utmost concern for electrospray spacecraft interactions are spacecraft charging and plume impingement [1]. The charged particles emitted by the thruster can return to the spacecraft, resulting in spacecraft charging and potential material erosion. The liquid-phase propellant and its conductivity also present

several further risks, as plume interception on spacecraft surfaces will not only result in spacecraft charging and surface removal, but chemical contamination as well [2]. Beyond these primary interactions, any surface impinged on by the plume will also be a potential site for the production of secondary species.

The purpose of this work is to develop a method for measuring the mass of secondary species produced by a primary electrospray plume impinging on a downstream surface. Previous work from the EP community has made progress in characterizing the emission of secondary charged species in electrospray material interaction [3, 4]. Contemporary studies have also attempted to characterize sputtering yields from bombardment by electrosprayed droplets rather than ion plumes [5–7]. However, potential secondary species include electrons, atomic and molecular ions, clusters, nanodroplets, as well as neutral pairs of deposited propellant or sputtered material from the impinged surface. The mass of these species and their angular distribution should be understood in order to understand potential facility effects arising from the deposition of secondary mass on experimental instruments. These results can also be used in attempts to improve existing models of plume-surface interactions and their consequences with regards to facility and spacecraft interactions.

III. Methodology

A. Molecular Dynamics Modeling Approach

The emissions produced by electrosprays are droplets and ions are on the nanoscale and are modeled through the Large-scale Atomic/Molecular Massively Parallel Simulator (LAMMPS), a molecular dynamics software package developed by Sandia National Laboratories [8]. These simulations were run in parallel on the Texas Advanced Computing Center's Stampede2 supercomputing cluster and involve an all-atom representation of 1-Ethyl-3-methylimidazolium tetrafluoroborate ([EMIM][BF$_4$]). The ionic liquid molecule is governed by Coulombic forces and Lennard-Jones 12-6 parameters obtained through the Lorentz-Berthelot mixing rules using parameters for the cation and anion from Kelkar et al. and Doherty et al., respectively [9][10] [11].

Since emissions are generated when the surface tension of the ionic liquid is broken, correctly reproducing surface tension values for [EMIM][BF$_4$] is essential to obtaining ion emission rates that reflect reality. In order to validate the surface tension of the bulk liquid, 1,000 [EMIM][BF$_4$] molecules are placed in a periodic simulation cell which is then equilibrated to 298.15 K. This initial bulk setup is shown in Fig. 1 (Left). As implemented by Doherty et al., the Kirkwood-Buff formula relates the pressure components on the ionic liquid to the surface tension and is given in Equation 1 [11]:

$$\gamma = \frac{1}{2}b_z\left(P_{zz} - \frac{1}{2}(P_{xx} + P_{yy})\right) \tag{1}$$

In LAMMPS, the pressure of the system is computed based on the methods of Thompson et al. by summing the forces on all of the atoms and dividing the total force by the volume of the simulation cell [12]. In this case, the length of the domain perpendicular to the liquid-vacuum interface (e.g., 320 Å) is the length, b_z, to be used in the Kirkwood-Buff formula. The surface tension computed with this formula for the system at 298.15 K was found to be 94.06 ± 10.93 $\frac{mN}{m}$, a value more than double accepted value of 44.3 $\frac{mN}{m}$ from literature [13]. According to Bhargava and Balasubramanian, their molecular dynamics simulations found that room temperature was insufficient to obtain properly converged liquid-vacuum interfaces thereby producing high surface tension values with large standard deviations [14]. In their study and in a subsequent paper by Doherty et al., these authors found that elevating the system temperature higher than 400 K produced surface tension values closer to experimental values[14] [11]. As a result, the 1,000 molecules are equilibrated and maintained at a temperature of 425 K which resulted in a surface tension of 48.00 ± 21.68 $\frac{mN}{m}$. Since this standard deviation is still relatively high, the number of molecules is increased to 4,000 which leads to a surface tension of 41.51 ± 7.30 $\frac{mN}{m}$, a value in agreement with experiments.
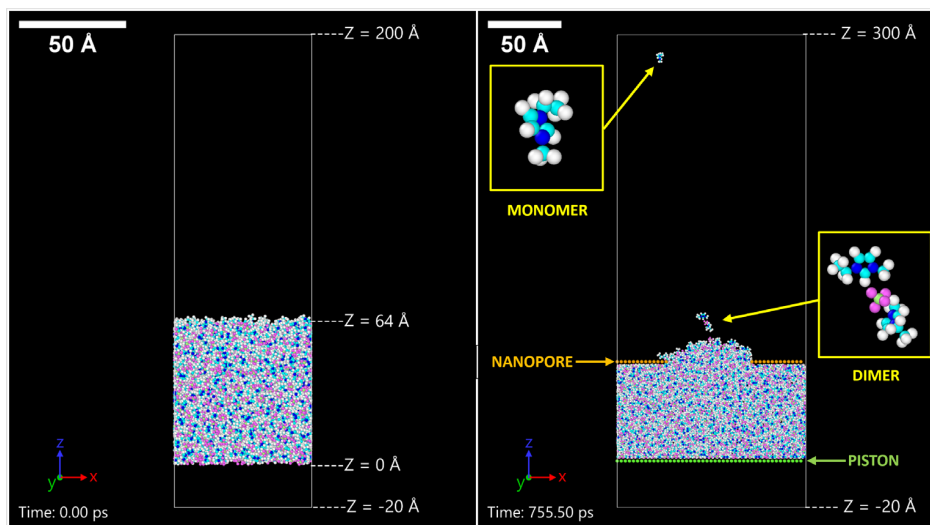
3

Figure 1   Bulk setup used to validate surface tension (Left) and piston-nanopore setup (Right)

With the surface tension validated, the piston-nanopore setup can be implemented at the elevated temperature. Based on previous work on simulating a bulk ionic liquid in the presence of a strong electric field, 4,000 ion pairs of the [EMIM][BF$_4$] propellant are placed in an approximately 127 Å x 127 Å x 320 Å simulation cell with periodic boundary conditions in its X- and Y-dimensions and fixed boundaries in its Z-dimension [9]. A rigid wall of 782 Platinum atoms is placed below the bulk ionic liquid to prevent it from leaving the system. The ionic liquid initially occupies the region from Z = -20 Å to about 64 Å with a vacuum occupying the remaining portion of the simulation cell. In order to reproduce the conditions at the tip of an emitter, a nanopore with a diameter half the size of the X-dimension of the simulation cell is placed 10 Å above the bulk ionic liquid. This piston-nanopore setup is based on the molecular dynamics simulation of Liu & Cao on measuring the surface tension of water [15]. The nanopore is given Lennard-Jones parameters that prevent the ionic liquid from interacting with and adhering to it. The ionic liquid is then equilibrated for 50 picoseconds under a canonical ensemble with a Nose-Hoover thermostat bring the system to the desired temperature. The piston and nanopore are initialized at rest and remain fixed in place throughout the equilibration period. The nanopore is assigned a spring force to keep these atoms in place throughout the simulation. An example of the piston-nanopore setup is shown in Fig. 1 (Right). At the end of the equilibration period, the density of the ionic liquid is verified to match experimentally obtained values for [EMIM][BF$_4$] by taking the average value across the 5-Angstrom bins that encompass the ionic liquid.

In an electrospray device, liquid is extruded through the emitter at a specified rate from a reservoir of propellant. Since molecular dynamics simulations are limited to nanoscale lengths and runtimes, these simulations only represent a portion of the emitter setup near its tip. As such, the temperature of the ionic liquid must be regulated when an electric field is applied to represent the reservoir which prevents the liquid from heating up rapidly. In order to maintain the desired temeprature while ensuring that the atoms are still capable of gaining enough energy to be emitted from the reservoir, a modified Nose-Hoover thermostat is implemented only in the X- and Y-dimensions to a portion of the bulk liquid. A microcanonical, NVE ensemble is applied to the rest of the system while the electric field is applied. After initial testing, the bottom 20-Angstrom layer of the liquid is found to maintain the temperature of the system while allowing the rest of the liquid to gain energy and produce emissions. Without this modification to the system, the temperature of the bulk increases rapidly when the electric field is applied leading to a collapse of the simulation. With this initial simulation setup, the electric field strength is then varied to build a relationship between these parameters and the resulting ion emission rates and currents.

In order to study the effects of the strength of the applied electric field on the ionic liquid, the currents for each emitted species can be computed. This is done by recording the number of each emitted species that exits the simulation cell, computing the total charge, and dividing by the change in time. After the 4,000 [EMIM][BF$_4$] molecules are equilibrated to 425 K, electric fields of 1, 2, 4, and 6 $\frac{V}{nm}$ are applied as the piston moves at approximately 0.02 $\frac{\text{Å}}{ps}$. This moving piston is meant to simulate the mass flow of the ionic liquid into the emitter over time that is seen in experimental systems [16]. This piston creates a pressure differential between the reservoir and the vacuum and causes the liquid to

4

flow above the nanopore to form and maintain a meniscus from which emissions are drawn by the applied electric field.

B. Experimental Approach

All experiments are conducted in a 24 " diameter by 27 " belljar vacuum chamber. The chamber is equipped with a Leybold DB16 rough vacuum pump and a CTI Cryo Torr 8 cryopump driven by a Brooks 9600 helium compressor. In this setup, the chamber has a base pressure of 6E-6 Torr, with all experiments conducted at operating pressures less than 1E-5 Torr, verified by a hot filament ion gauge.

The electrospray thruster used in these experiments is based on the AFET porous glass thruster designed by AFRL [17, 18]. Current emission characteristics and an energy distribution for the thruster were collected using a retarding potential analyzer (RPA) and Faraday cup. The thruster was operated by applying a high positive or negative voltage to two electrodes contacted to the emitter array and extractor grid. The difference between the emitter and extractor voltage represented the extraction potential, while the ions in the extracted plume would have an energy equivalent to the bias placed on the emitter. Current output from the emitter and current received by the extractor were measured by individual evaluation modules consisting of a Texas Instruments AMC1311 isolation amplifier and a 1kΩ shunt resistor. Target current were measured by a Keithley 6514 electrometer across a 1kΩ shunt resistor. Plume energy diagnostics were conducted using a Kimball Physics Faraday cup with RPA grids. The current measured at the Faraday cup was collected by the Keithley electrometer. All data was passed through a National Instruments USB 6211 DAQ.

The mass of secondary particles emitted from the bombarded surface was measured using a quartz crystal microbalance (QCM). Studies conducted by Williams et al. demonstrated the use of a QCM to collect mass removed from the surface of a target bombarded by xenon ions at incremental polar angles from the target surface normal [19]. Figure 2 shows the setup used in these experiments with the porous glass thruster as the ion source, with dimensions given in Fig. 2b. The downstream target was a sheet of polycrystalline nickel. Though not as prevalent as aluminum or steel alloys in spacecraft and experimental facilities, nickel is a readily available, non-alloyed material, which would make for simpler comparison with established values.
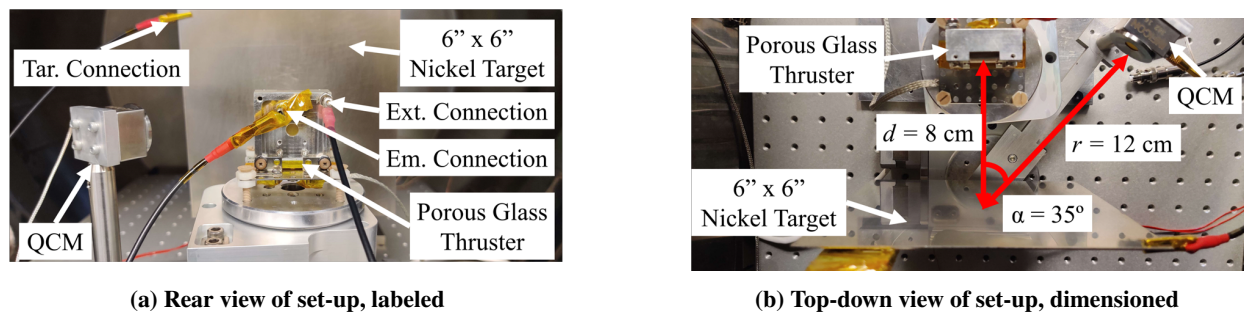

(a) Rear view of set-up, labeled

(b) Top-down view of set-up, dimensioned

Figure 2   Experimental set-up for measuring secondary mass flux yields

The microbalance used in these experiments was a front load crystal QCM with an Inficon XTC/3S Deposition Controller. Inficon Gold-Coated 6MHz quartz crystals were used as the receiver for superior adhesion when compared to bare quartz crystals or alloy-coated crystals. Figure 3 shows the exact sensor used in the experiments with the specified crystal loaded. In this configuration, the exposed area of the crystal was measured to be 1.593 cm^2. The QCM was mounted on a Newmark Systems RM-3 rotary stage in order to allow the probe to measure the yield at a range of polar angles.
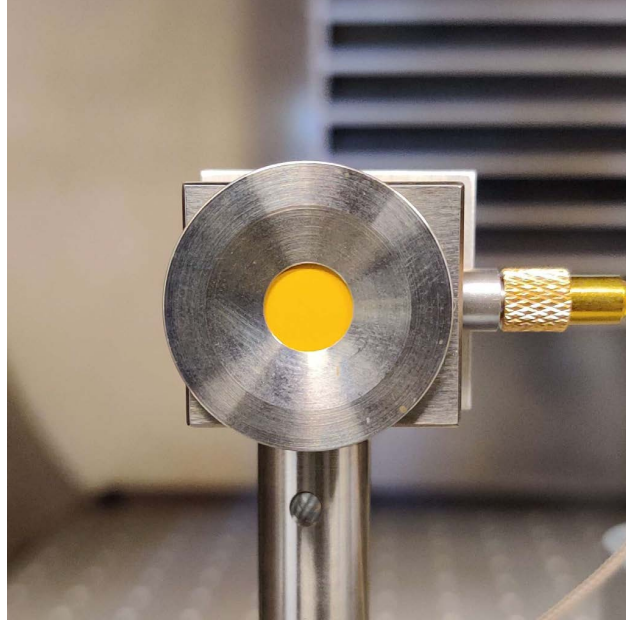
Figure 3   Inficon Front-load QCM used in deposition experiments

The QCM applies a high frequency oscillation to a cut quartz crystal as a thin film of sputtered mass deposits on it and measures the change in the resonant frequency. The correlating change in mass can then be calculated according to the Sauerbrey equation. The constant C is the mass sensitivity constant, cited as $12.35 \frac{\text{ng}}{\text{Hz}-2}$ for 6MHz crystals, and n is the film overtone number, assumed to be $n = 1$ for monofilm deposition [20]. The deposition rate $\frac{dm}{dt}$ is then used to determine the secondary mass flux yield, $y(\alpha)$ based on the plume current J and charge q of the primary plume ions, as well as the collector distance r and area A_s.

$$\frac{\mathrm{d}m}{\mathrm{d}t} = -CA_\text{S} \frac{1}{n} \frac{\mathrm{d}f}{\mathrm{d}t} \tag{2}$$

$$y(\alpha) = \frac{\frac{dm}{dt} q r^2}{J A_S} \tag{3}$$

IV. Results & Discussion

A. Molecular Dynamics Modeling Results

Changing the electric field strength enables the development of a relationship between with the emission rate. In these molecular dynamics simulations, 4,000 [EMIM][BF$_4$] molecules are equilibrated for 50 piscoseconds before an electric field is applied for 1 nanosecond while the piston moves at $0.02 \frac{\text{Å}}{ps}$. The moving piston velocity corresponds to the pressure differential in an electrospray device produced as the propellant is extruded through the emitter. A modified Nose-Hoover thermostat applied to the bottom 20-Angstrom layer successfully allows the system temperature to increase gradually while maintaining the bulk ionic liquid at approximately 425 K. With a microcanonical ensemble applied to the rest of the system, the electric field is varied. Values of 1, 2, 4, and 6 $\frac{V}{nm}$ are tested to find the resulting species emission rates and currents.
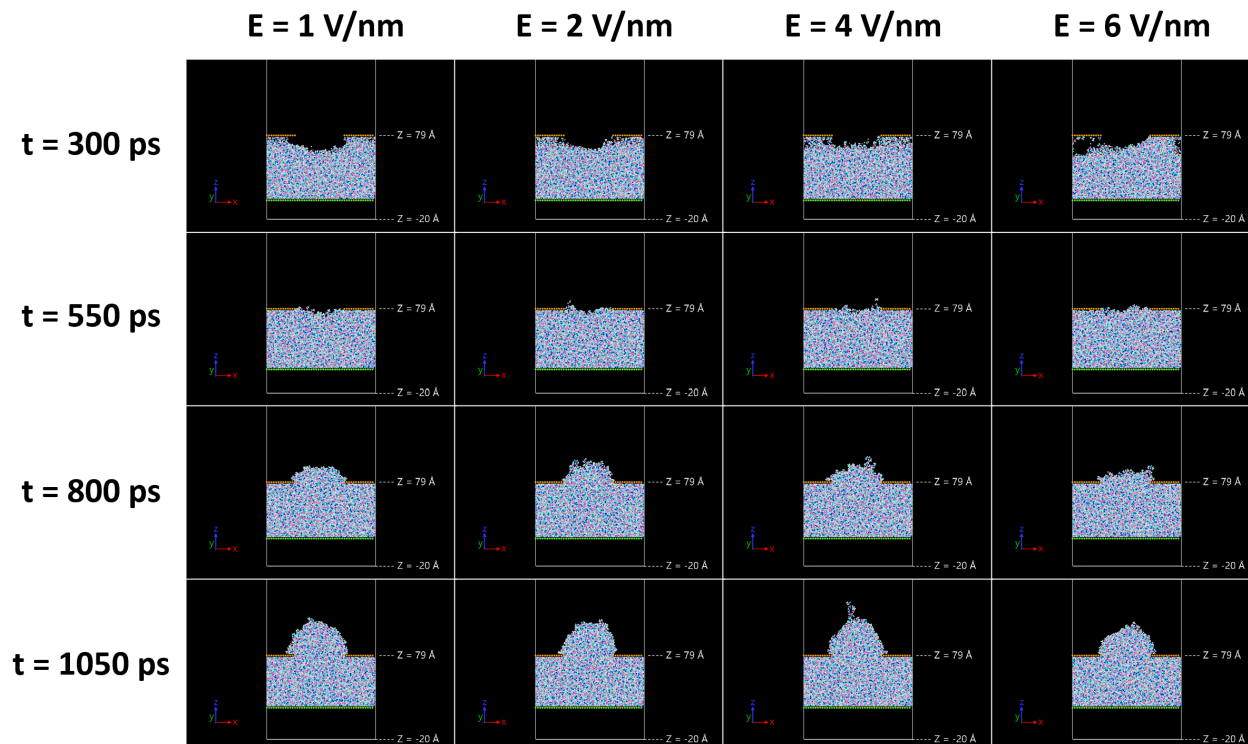
Figure 4   Snapshots of ionic liquid in piston-nanopore setup over time after application of E-field

Snapshots of the piston-nanopore simulations over time are shown in Fig. 4 where each column corresponds to an applied electric field strength. In previous simulations, a field of 6 $\frac{V}{nm}$ was required to produce significant emissions; however, this also produced shock waves that generated transient emissions due to the sudden acceleration of the molecules from their initial velocities after equilibration [9] [21]. In all cases, menisci of similar heights have formed over the nanopore by 800 picoseonds into each piston-nanopore simulation. The 6 $\frac{V}{nm}$ meniscus at 800 picoseconds appears to be less defined that the others and may be due to the relatively high number of transient emissions that occur prior to the formation of the meniscus. This leaves fewer molecules to be extruded by 800 picoseconds. As opposed to previous simulations where these transient emissions ocurred almost as soon as the electric field was applied, the initial emissions in the piston-nanopore simulation appear to be more gradual [9]. Further investigation is required to determine what portion of these initial emissions may be transient and need to be excluded from total species counts Through this piston-nanopore simulation setup, the required electric field strength to produce emissions is reduced to a value closer to the 1 $\frac{V}{nm}$ critical value observed experimentally for similar ionic liquids [22]. These results demonstrate the importance of the formation of a well-defined meniscus with regard to the production of emissions at lower applied electric field strengths and is an important step toward modeling real electrospray emitters.

At 1 $\frac{V}{nm}$, a single trimer is emitted from the tip of the meniscus that forms as the ionic liquid is extruded by the moving pistons. This emission may be due to statistical variations in the energy of the system and is expected as this field strength is at or below the accepted threshold to produce emissions [22]. With an electric field strength in excess of 2 $\frac{V}{nm}$, the meniscus appears to transition to a Taylor Cone prior to producing emissions. This transition is particularly evident by comparing the 800 and 1050 picosecond snapshots for the 4 $\frac{V}{nm}$ case in Fig. 4 where the 1050 picosecond case has developed a sharper tip where an emission appears. At 2 $\frac{V}{nm}$, a total of 20 emissions are produced with the majority being cation and dimer emissions. Heavier species remained at 0 or 1. As the field is doubled again to 4 $\frac{V}{nm}$, the number of emissions increases by 150% to a total of 50. In Fig. 1 (Right), a snapshot of the 4 $\frac{V}{nm}$ case taken at 755.50 picoseconds is shown with an example of the monomers and dimers emitted from the tip of the meniscus once the electric field is applied. In this case the number of cations emitted increased from 10 to 40 while the number of dimers remains at 9, comprising less of the total number of emissions. One or fewer emissions is generated at 2 $\frac{V}{nm}$. Finally, when the electric field strength is increased to 6 $\frac{V}{nm}$, the number of emissions increase by about 72% to a total of 86 emissions. Once again the majority of the emissions are the 76 cations. These counts can then be converted to

7

currents and recorded cumulatively over time. The resulting species currents are shown as functions of the electric field strength in Fig. 5
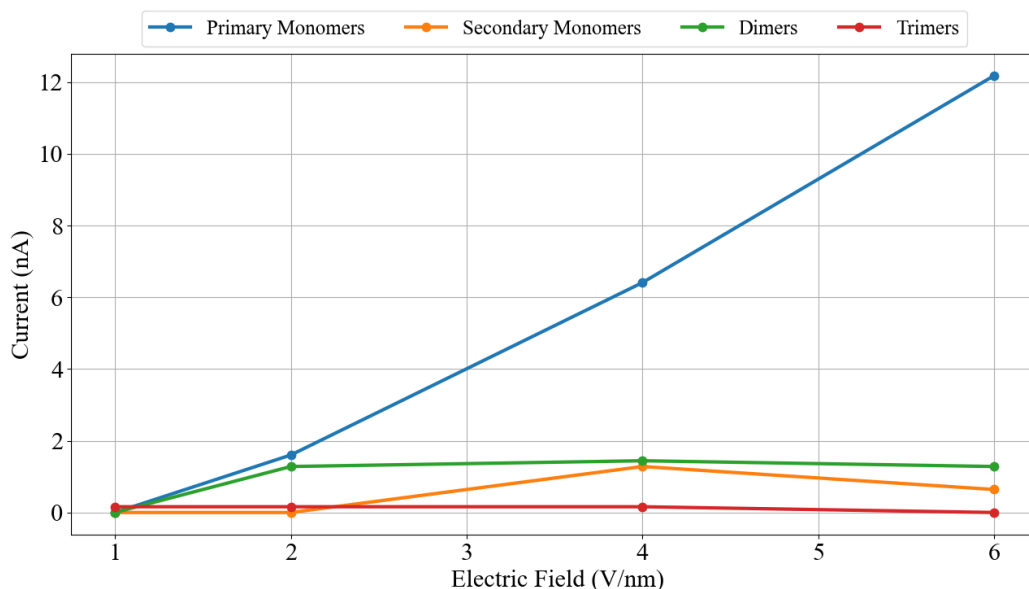

Figure 5   Average current over 1 nanosecond as a function of the applied electric field strength

In Fig. 5, the average primary monomer current increases monotonically in a nearly linear relationship with the applied electric field strength. At $1 \frac{V}{nm}$, all currents are less than 2 nA. In the $2 \frac{V}{nm}$ case, all of the cations produced are primary emissions. In the 4 and $6 \frac{V}{nm}$ cases, 8 and 4 of the total number of cation emissions for each case are secondary emissions produced by fragmentations of heavier species. The products of fragmentation consist of an ion and a neutral pair that may drift off-axis or are not capable of being accelerated further by the electric field, respectively. These secondary ion and neutral pair emissions can reduce the efficiency and lifetime of the device. These molecular dynamics simulations demonstrate that the piston-nanopore setup can reliably produce emissions once the theoretical threshold of 1 to 1.5 $\frac{V}{nm}$ is exceeded. In previous bulk setups where the ionic liquid is left in the reservoir without a piston to extrude it, electric field strengths in excess of $2 \frac{V}{nm}$ are needed to produce emissions for the [EMIM][BF$_4$] [21]. By extruding the propellant with the moving piston and an applied electric field, the ionic liquid meniscus and the surface tension is maintained as ions are extracted from the tip of the emitter.

The results of Liu & Cao appear to demonstrate boundary effects that are evident in the shape of the meniscus that forms [15]. The meniscus becomes detached from the surface surrounding the nanopore. This is possibly the result of the interaction between the ionic liquid and its periodic images or the Lennard-Jones parameters that define the interaction between the ionic liquid and the nanopore. In order to investigate these effects, the system will need to be scaled, pushing these simulations to the limits of molecular dynamics simulations in terms of computational costs. Since electrospray thrusters are orders of magnitude larger than can be modeled by nanoscale molecular dynamics simulations, it will also be necessary to scale these simulations to obtain emission rates and currents that can be compared with the experimental data. These results show that cation emissions increase almost linearly as a function of the applied electric field strength. The piston-nanopore setup produces emissions even for applied field strengths closer to the critical value of 1 or 1.5 $\frac{V}{nm}$ seen in literature whereas previous bulk setups did not. Through techniques such as coarse-graining which reduce the number of particles needed to represent an [EMIM][BF$_4$], it will be possible to scale this setup to time- and length-scales that better reflect reality. In doing so, the aim will be to obtain more accurate, high-fidelity emission and fragmentation rate data that can be used to inform larger time- and length-scale simulations such as particle-in-cell which can access more realistic domain sizes. With these improvements and access to larger time- and length-scales, the aim is to produce a model that is capable of capturing the ion emission and fragmentation rates as seen in experiments.

8

B. Experimental Results and Discussion

1. Primary Plume Characterization

Primary plume diagnostics for the porous glass thruster were conducted prior to evaluating the secondary mass flux. Figure 6 shows anion and cation current-voltage curves for the thruster loaded with [EMIM][BF$_4$]. These curves were collected by fixing the extractor potential at ground, and sweeping the emitter bias from 0 V to 2000 V in a 1 Hz triangle wave while measuring current at the emitter, extractor, and a collector plate downstream of the thruster.
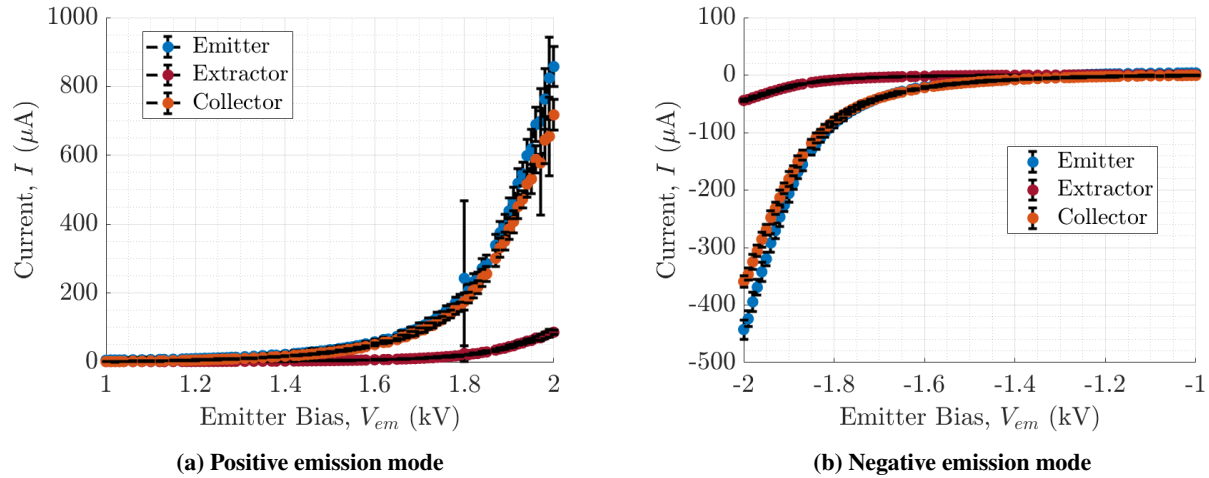

(a) Positive emission mode   **(b) Negative emission mode**

Figure 6   Characteristic current-voltage curves for a porous glass thruster spraying [EMIM][BF$_4$]

Figure 7 shows cumulative energy spectra for positive and negative electrospray plumes produced with the porous glass thruster. These curves were collected by operating the thruster in a 1 Hz bipolar square wave with a magnitude of 1.9 kV, while the RPA grids swept in a 0.5 HZ triangle wave, sweeping from 0 V to 2 kV. The current in each mode was averaged across 50 sweeps, and the averaged results were normalized by the maximum value in either mode. The spectra indicate the plume is composed of 80% singly charged cations when biased positively and 70% singly charged anions when biased negatively. Drops in current in the field free region are indicative of a small but not insignificant fraction of fragmenting dimers and trimers. These results also show an increasing signal at low suppression voltages in both spectra. Similar behavior was seen in RPA spectra obtained by Bruno et al. in a recent study characterizing electrospray thrusters with [EMIM][BF$_4$] and several hydroxylamine nitrate (HAN) based propellants sprayed with an iEPS porous glass thruster [23].
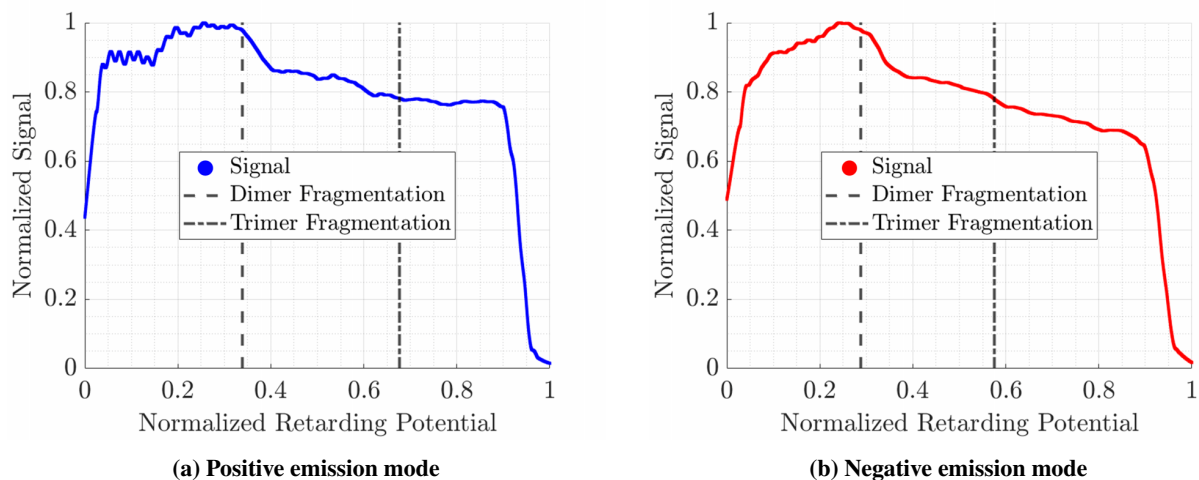
9

(a) Positive emission mode

(b) Negative emission mode

Figure 7   Cumulative energy spectra for an [EMIM]$[BF_4]$ electrospray plume produced with a porous glass thruster

2. Measurements of Secondary Mass Flux Yield

QCMs are well-characterized instruments used commonly in a variety of thin film deposition systems for measuring and monitoring purposes. For these experiments, no mass calibration was conducted using a known mass deposition source; instead, the mass sensitivity constant given by the crystal manufacturer was used for mass determination. Additional characterization was completed to assess the instrument's performance in this particular experimental setup and design the experimental procedure to best accommodate the sensor's functionality and produce repeatable results.

In these initial experiments, the QCM's polar position was fixed at $35°$. Three deposition events were conducted in a single chamber pump-down with the same QCM crystal. In each deposition, the primary plume impinging on a nickel target was produced by the same porous glass thruster operating with a grounded extractor and the emitter biased to $±1900$ V. The thruster was operated in a 1 Hz square wave bipolar mode to ensure maximum operating time, as previous tests with the thruster in monopolarity showed a sharp decline in primary plume current over time and a propensity for shorting and arcing between the emitter and extractor. Each deposition took place over 60 minutes, and 60 minutes of "settling" time was taken in between each deposition phase to allow the QCM to reach a steady state after each deposition. Figure 8a shows the frequency traces from each test with traces before and after the deposition phase included. The cumulative mass deposition $\sum_{t=0}^{t_{\text{off}}} \frac{\mathrm{d}m}{\mathrm{d}t}$ over time is plotted for each test in Fig. 8b, and Fig. 8c shows the frequency results normalized along both axes. Raw current and voltage traces from 5 seconds of the second deposition test are shown in Fig. 8d.
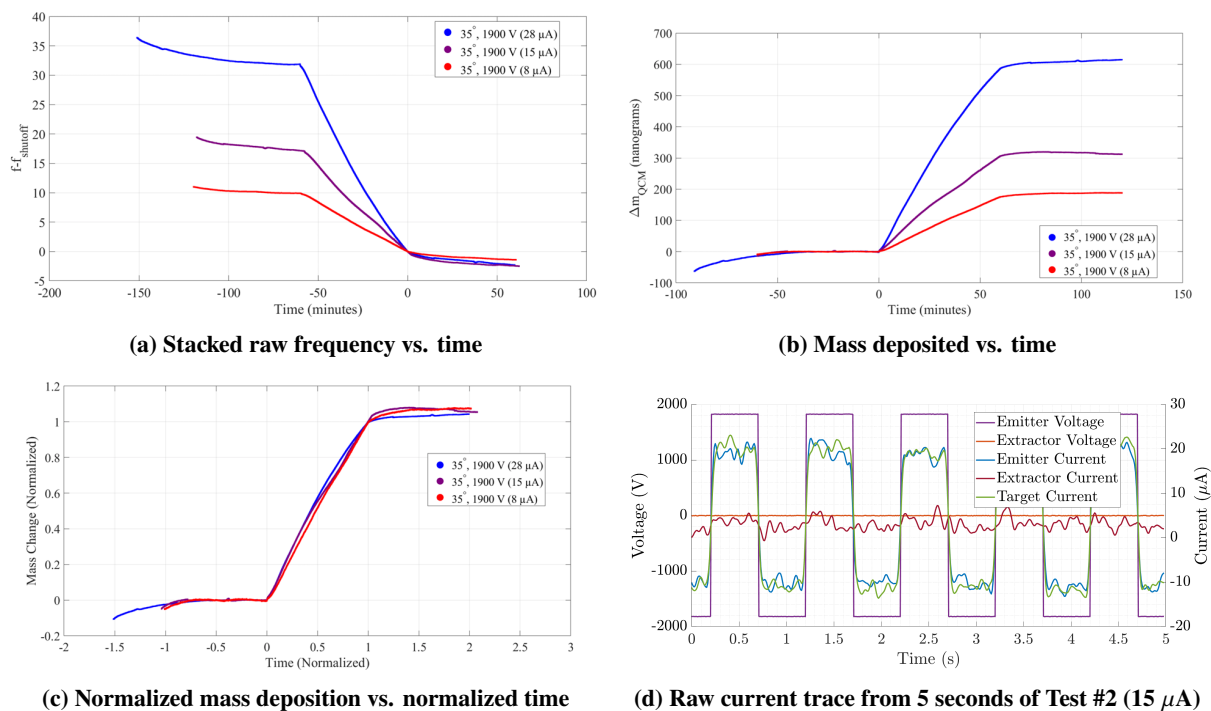
10

(a) Stacked raw frequency vs. time

(b) Mass deposited vs. time

(c) Normalized mass deposition vs. normalized time

(d) Raw current trace from 5 seconds of Test #2 (15 μA)

Figure 8   Raw frequency and current data prior to processing

The raw target current I_{tar} was averaged over each 0.5 second pulse in each polarity. Given that the QCM only logged frequency every one second, the current data had to be further processed to directly compare the two values and calculate a single value for mass flux yield over a given time interval. The pulse-averaged frequency and current data were individually interpolated onto uniform time arrays such that one $\frac{dm}{dt}$ data point corresponds to the pulse averaged I_{tar} value at that same time interval. The mass flux yield y was then calculated according to Equation (3). Figure 9 shows the calculated yield values over time for all three tests.
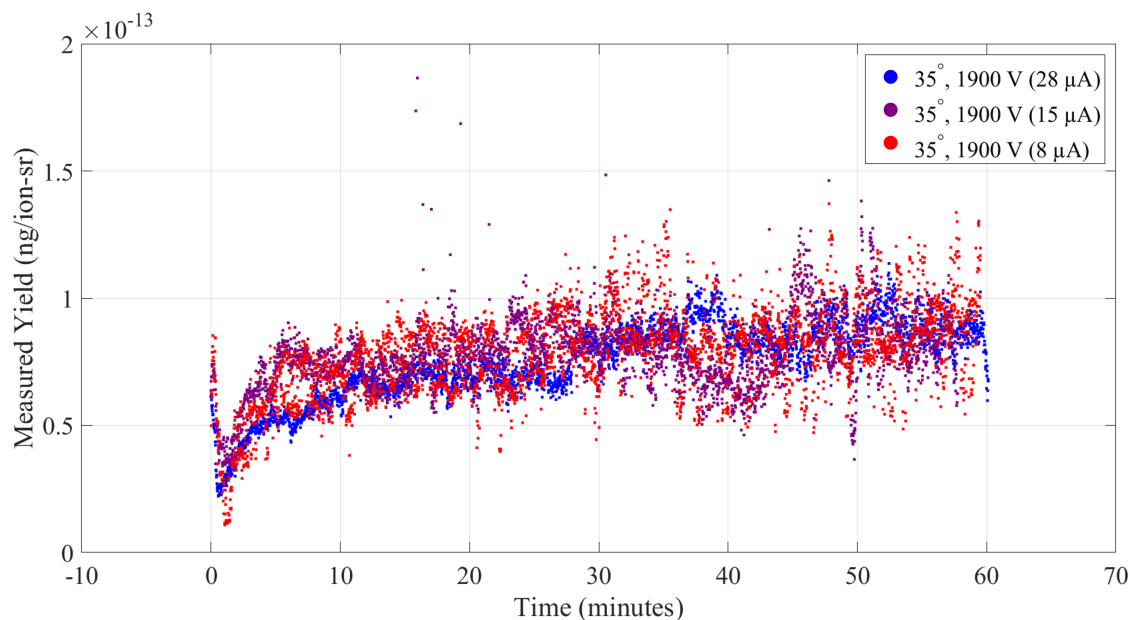

Figure 9   Secondary mass flux yield vs time

11

Note the transience in the mass flux yield values in the first ~15 minutes of deposition. This transience is likely attributable to a combination of thermal effects and thin film formation. As the secondary particles accumulate on the surface of the crystal, they deposit a small amount of energy onto the sensor and disrupt the thermal equilibrium the sensor was in prior to spraying. Additionally, the film developing on the crystal is not an immediate monolayer. Only when the particles have formed a relatively uniform film covering the total exposed surface area does the resonant frequency of the crystal change proportionally to the mass per unit area. As a result, only the mass flux yields after the transience appears to have settled to a steady state — ~15 minutes in these tests — are considered representative of the actual values. Table 1 presents the average of $\{y|t > 15 \text{ min}\}$ for each of the three deposition tests. Note that values are expressed to four significant figures, as the reported mass sensitivity constant limits the precision with which values can be provided with confidence.

Table 1   Average secondary mass flux yields at constant energy and polar angle

Test #	$|y|(\frac{\text{ng}}{\text{ion-sr}})$	$\sigma(\frac{\text{ng}}{\text{ion-sr}})$
1 (28 μA)	7.992×10^{-14}	1.132×10^{-14}
2 (15 μA)	8.017×10^{-14}	1.319×10^{-14}
3 (8 μA)	8.205×10^{-14}	1.157×10^{-14}

The cumulative average and variance for these three yields are then $\bar{y} = 8.07 \times 10^{-14} \frac{\text{ng}}{\text{ion-sr}} \pm 1.16 \times 10^{-15} \frac{\text{ng}}{\text{ion-sr}}$. Given the low cumulative variance in these values, the method was deemed repeatable and further testing applying the process was completed.

3. Dependence on Nominal Energy of Primary Plume Ions

Applying the method detailed above, the energy dependence of secondary mass flux yield was evaluated. The polar position in these tests was once again fixed at 35°. Five test points on a range of energies on $V_{\text{pri}} \in [250, 2500]$ V were determined in order to cover an order of magnitude of primary plume energies. To account for the limited operating range of the thruster, the extractor was not fixed at ground, but was instead allowed to be biased in a 1 Hz square wave mode in sync with the emitter bias. For example, if the goal was to produce a ±500 V primary plume, but the thruster was producing a stable plume at an extraction potential of ±2000 V, the emitter was biased to ±500 V in a 1 Hz square wave, while the extractor was biased to ∓1500 V in a 1 Hz square wave phase shifted by 180° from the emitter square wave. The emitted plume will have a nominal potential of 500 V relative to the grounded target and chamber, but will still be extracted from the thruster as if it was operated in standard conditions. Tests were conducted at high voltages first, and decreased in log spaced increments down to the low voltage in each sequential deposition phase. Figure 10 shows the frequency traces for the full test range.
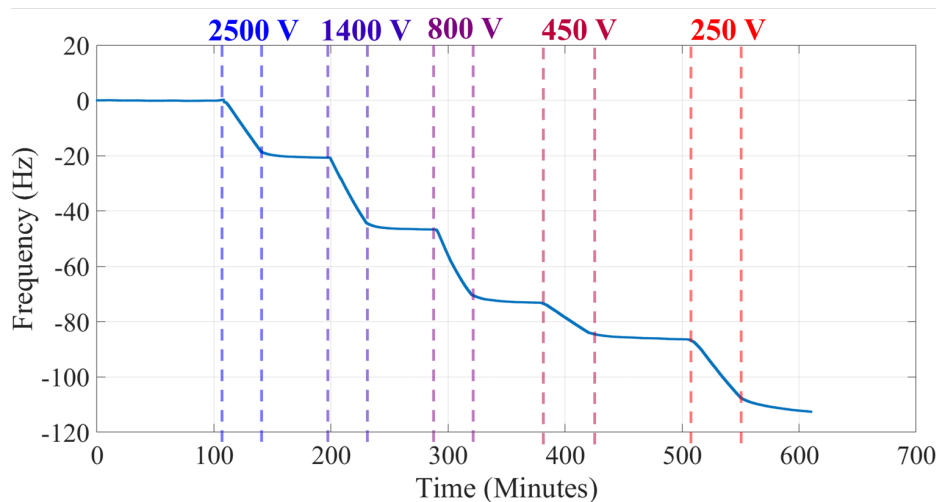

Figure 10   Raw frequency traces from energy dependence tests

Processing the frequency and current data using the previously discussed method, the yield values were calculated for each test and plotted as shown in Fig. 11.
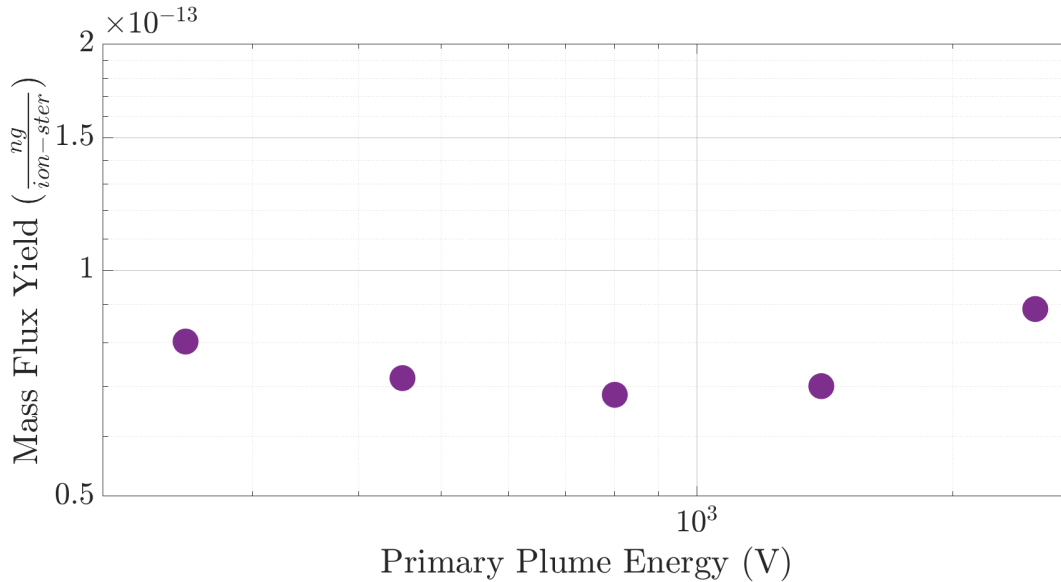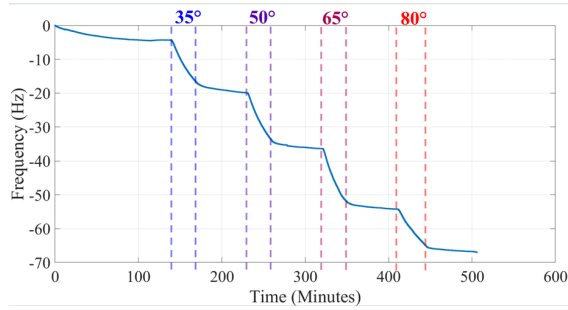

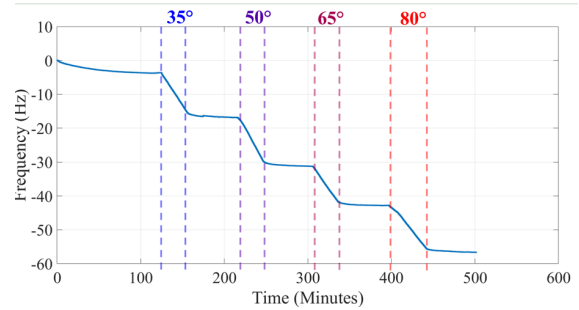**Figure 11   Calculated secondary mass flux yield vs nominal primary plume energy**

These results show that the secondary mass flux yield exhibits little change across the range of primary energies, aside from slight increases at the lower and upper bounds. This trend contradicts established values for sputtered nickel. If carbon impacts nickel at normal incidence on the range of $V_{pri} \in [27, 270]$ eV, one would expect the yields increase logarithmically as shown by Ref. [24]. Sputtering yields for most single knock-on collisions presented by Bohdansky are shown to increase as primary energy increases, with a maximum reached on the order of 10^3 eV followed by a decrease in yield at much higher energies ($> 10^4$ eV) [25, 26]. The results obtained in this study however, show little change with energy, aside from slight increases at the lowest and highest tested energies. If this small variance is attributed to the uncertainty in measurements arising from the mentioned thermal effects, then it can be presumed that the yield did not change appreciably over this range.

4. Angular Profile of Secondary Mass

Profiling the angular distribution of secondary mass was the goal for the next round of experiments. These tests consisted of operating the thruster at one condition across deposition events, while moving the QCM to different polar positions as shown in Fig. 2. Given the results described above, the angular profile was obtained for two different plumes: a low voltage plume produced by a thruster with a biased extractor, and a high voltage plume produced by a thruster with a grounded extractor. Figure 12 shows the raw frequency data collected to obtain the angular profiles.

13

(a) Low voltage plume

(b) High voltage plume

Figure 12   Raw frequency traces collected to develop angular profile of secondary mass

Figure 13 shows the calculated mass flux yields alongside cosine distributed sputtering yields for carbon incident on nickel, as well as total and partial backscattered carbon. The theoretical yields were obtained using SRIM, and assumed to be cosine distributed [25, 27].
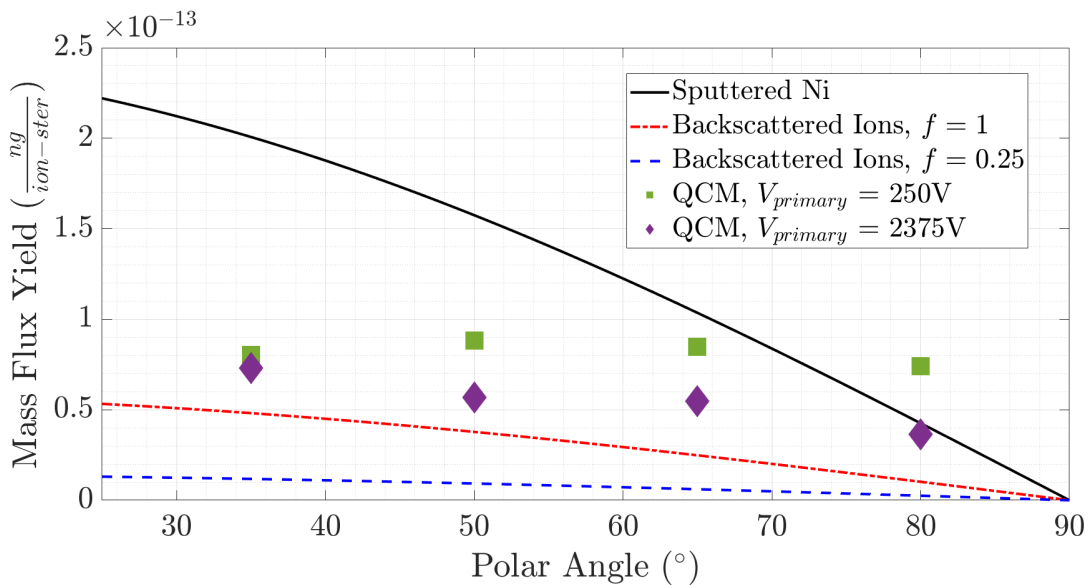

Figure 13   Calculated secondary mass flux yield profiles compared with cosine distributed sputtering and backscattering profiles

The high voltage secondary yields underestimate sputtered nickel and overestimate both 25% backscattering and total reflection. If the given model for secondary particle production holds, it can be posited that the sputtering and backscattering are both contributing to the measured mass deposition when spraying a high voltage primary plume with a grounded extractor. However, the low voltage primary plume does not result in yields that reflect any of the literature or models available. This confounding result indicates that the measurements observed may be affected by variables which are not accounted for in the experimental design.

C. Additional Variables Influencing Measured Yields

The measured yields from these experiments were shown to be repeatable and consistent, but the expected angular distribution of secondary mass and energy dependency of secondary flux was not observed. In order to contextualize these results and motivate future research in this area, potential factors which may have influenced the results without being accounted for in the experimental design were proposed and analyzed.

14

1. Effects of Extractor Biasing

While the secondary mass flux yield angular distribution reflected some aspect of expected values for a high voltage primary plume, the angular profile for secondary mass from a low voltage plume appeared constant across a range of angles. Varying the energy of the primary plume also did not result in the predicted change, which could indicate a strong contribution from backscattering; however, when considering this result in concert with the aberrant angular profile from the low voltage plume, a better explanation for these results may lie in the experimental method used to produce primary electrospray plumes with a broader range of energies. The porous glass thruster used in these experiments only operates in a small range of emitter voltages when holding the extractor at ground. In order to produce a larger range of voltages to better represent the research interests and motivations, the operation procedure for the thruster was modified to change the extractor voltage in sync with the emitter voltage. However, no further changes were made to the thruster layout or experimental method in order to compensate for the structure of the electric field downstream of the thruster.

Much of the literature and accepted convention for electrospray thrusters and electrospray material interactions make clear that there is a "field-free" region outside of the thruster [5, 28, 29]. When not holding the extractor at ground, there is a potential differential between the extractor and the downstream target, resulting in an electric field that is relatively weak in comparison to the electric field applied to produce the plume, but not so weak as to be negligible. It is also worth noting that the extractor is electrically connected to the aluminum thruster housing. As a result, in many of these tests, there was a large surface area of charged surface that could attract or repel charged species outside of the thruster. It is possible that due to the proximity of the thruster to the QCM in these experiments, the interactions between the charged species and the thruster exterior is impacting the secondary plume and the charged mass depositing onto the QCM. As a result, the yield values obtained in experiments with a biased extractor are not comparable to models of sputtering or backscattering, and should be limited in their consideration until improved experiments with a "cleaner" electrical environment can be conducted. One way of producing this "cleaner" environment would be to cage the thruster in a grounded shell, with an aperture to permit the plume ions to extract unimpeded. Figure 14 shows a simple sketch of how the current test setup could be modified to achieve this.

2. Angular Effects

The divergent plume produced by the porous glass thruster may have also contributed to the inconsistent results. Studies on sputtering from ion beams have shown that sputtering yields and angular distributions of secondary mass tend to be strong functions of primary incidence angle [19, 30, 31]. In the experiments detailed here, the distribution of the primary plume was not controlled, and as a result, some primary ions struck the nickel target at normal incidence at the center of the target, while other ions would reach a point on the target 2 to 5 cm away from the center at a glancing angle. This lack of control over impact site and impact angle could be one reason the angular distributions do not track well with either the cosine distributed sputtering or backscattering yields. Cosine distributions make an assumption that the plume ions impact at a single point with normal incidence. In order to better compare these results, the plume should be collimated into a unidirectional beam using an electrostatic lens. Using a device much like the one detailed in Ref. [32], a divergent electrospray plume can be collimated to a fine beam with minimal angular components without significantly changing the energetic distribution of the constituent ions. See Fig. 14 for an example of how this device could be implemented in the existing setup.

3. Thermal Drift

The quartz crystal microbalance used in these experiments was sensitive to changes in temperature. The background drift as observed in all the QCM frequency traces is likely a result of drifting temperature while instrument electronics settle to a steady state. The results presented were collected intermittently to allow the sensor to reach a steady temperature before starting any deposition, but the thermal effects during deposition were not accounted for with any active cooling or temperature compensation. Several techniques exist to address thermal transience during deposition. Many models of QCMs include fluid lines to pass a liquid around the sensor head to carry away any heat that is transferred to the crystal while mass is being deposited [20]. By doing this, changes in sensor temperature are less pronounced, and the resultant drift is reduced. Other methods include using two crystals in a thermoelectric quartz crystal microbalance (TQCM) [33]. This setup exposes one crystal to the test environment, while keeping the second crystal isolated from the deposition process. By observing the frequency difference between the two oscillators, the effects of the deposition can be separated out from the thermal background effects. To improve upon the results obtained in these experiments, a cooled QCM — as indicated in Fig. 14 — should be utilized in following investigations.
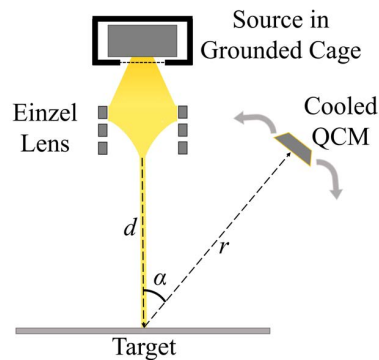
15

Figure 14   Proposed setup for modified tests

V. Conclusion

Through these simulations, it becomes clear that the rate of ion emissions is a function of the electric field strength and that the pressure difference across the meniscus aids in driving ion emissions by maintaining surface tension. When a critical electric field strength is applied, ions are emitted from the tip of the convex meniscus. At the molecular dynamics scale, it is possible to resolve the species emitted along with the products of any fragmentation events that occur. Improving the ability to predict emission rates as a function of variables such as the pressure associated with a mass flow rate, or the strength of the applied electric field is important in offering guidance in designing electrospray systems. Unlike models at larger scales, a molecular dynamics model is at the atomic scale and allows one to resolve the species emitted over time. This is important as charged species may return to regions surrounding the emitter and potentially erode these surfaces. Overall, these results demonstrate that molecular dynamics can be utilized to model electrospray systems at the atomic scale while reproducing properties such as the density or behaviors such as the formation of a Taylor Cone that are observed at larger scales. When used in combination with course-graining techniques that reduce the all-atom representation of the molecule to several interactions sites, the results of these simulations can be used to inform models at larger scales. The ability to predict the emission rates and emitted species using larger-scale models informed by these molecular dynamics simulations can enable the development of more efficient propulsion systems based on adjustable parameters like the electric field strength or the resulting pressure differential.

Secondary mass flux yields from a primary electrospray plume impinging on a polycrystalline nickel surface were measured using a quartz crystal microbalance. Initial diagnostics on the porous glass thruster used to produce the plume were conducted. Confounding results and inconsistency with expected values suggests that additional factors must be considered in future experimental designs. Regardless of this limitation, the angular profile represents a useful initial step in characterizing the plume-surface interactions for electrospray thrusters. These results can be used by experimentalists to aid in experimental design and measurement corrections. Modelers focused on electrospray systems can use this work and future improvements to better predict electrospray thruster performance and better anticipate thruster spacecraft interactions. Limitations of this study should be addressed by altering the thruster design to insulate the extractor from the thruster body, and minimizing the effects of the biased extractor by placing the thruster in a grounded cage or adding a grounded grid downstream of the extractor. Improved results could also be obtained by implementing a similar setup with a cooled QCM to minimize thermal effects. Future work on this topic should isolate the effects of positive plumes and negative plumes by filtering the primary plume by polarity or using a thruster that can operate in a single polarity for extended amounts of time. Experiments should also characterize the effects of impact angle by collimating the plume into a equipotential beam using an Einzel or electrostatic lens.

VI. Acknowledgements

References

[1] Mier-Hicks, F., and Lozano, P., "Spacecraft-Charging Characteristics Induced by the Operation of Electrospray Thrusters," *Journal of Propulsion and Power*, Vol. 33, No. 2, 2017, pp. 456–467. https://doi.org/10.2514/1.B36292.

[2] Thuppul, A., Wright, P. L., Collins, A. L., Ziemer, J. K., and Wirz, R. E., "Lifetime considerations for electrospray thrusters," *Aerospace*, Vol. 7, No. 8, 2020, pp. 1–18. https://doi.org/10.3390/AEROSPACE7080108.

[3] Klosterman, M. R., Rovey, J. L., Levin, D. A., and Rao, A., "Ion-induced charge emission from unpolished surfaces bombarded by an [Emim][BF4] electrospray plume," *Journal of Applied Physics*, Vol. 131, No. 24, 2022. https://doi.org/10.1063/5.0060615.

[4] Uchizono, N. M., Collins, A. L., Marrese-Reading, C., Arestie, S. M., Ziemer, J. K., and Wirz, R. E., "The role of secondary species emission in vacuum facility effects for electrospray thrusters," *Journal of Applied Physics*, Vol. 130, No. 14, 2021. https://doi.org/10.1063/5.0063476.

[5] Gamero-Castano, M., and Hruby, V., "Electrospray as a Source of Nanoparticles for Efficient Colloid Thrusters," *Journal of Propulsion and Power*, Vol. 17, No. 5, 2001, pp. 977–987. https://doi.org/10.2514/2.5858, URL https://doi.org/10.2514/2.5858.

[6] Gamero-Castaño, M., and Mahadevan, M., "Sputtering of silicon by a beamlet of electrosprayed nanodroplets," *Applied Surface Science*, Vol. 255, No. 20, 2009, pp. 8556–8561. https://doi.org/10.1016/j.apsusc.2009.06.018.

[7] Borodin, D., Brezinsek, S., Miettunen, J., Stamp, M., Kirschner, A., Björkas, C., Groth, M., Marsen, S., Silva, C., Lisgo, S. W., Matveev, D., Airila, M., and Philipps, V., "Determination of Be sputtering yields from spectroscopic observations at the JET ITER-like wall based on three-dimensional ERO modelling," *Physica Scripta*, Vol. T159, 2014. https://doi.org/10.1088/0031-8949/2014/T159/014057.

[8] Thompson, A. P., Aktulga, H. M., Berger, R., Bolintineanu, D. S., Brown, W. M., Crozier, P. S., in 't Veld, P. J., Kohlmeyer, A., Moore, S. G., Nguyen, T. D., Shan, R., Stevens, M. J., Tranchida, J., Trott, C., and Plimpton, S. J., "LAMMPS - a flexible simulation tool for particle-based materials modeling at the atomic, meso, and continuum scales," *Computer Physics Communications*, Vol. 271, 2022, p. 108171. https://doi.org/https://doi.org/10.1016/j.cpc.2021.108171, URL https://www.sciencedirect.com/science/article/pii/S0010465521002836.

[9] Azevedo, V. A., "Molecular dynamics simulations of EMIM - BF4 ionic liquid for electrospray thrusters," Master's thesis, University of Illinois Urbana-Champaign, 2021. URL https://hdl.handle.net/2142/113004.

[10] Kelkar, M. S., Shi, W., and Maginn, E. J., "Determining the Accuracy of Classical Force Fields for Ionic Liquids: Atomistic Simulation of the Thermodynamic and Transport Properties of 1-Ethyl-3-methylimidazolium Ethylsulfate ([emim][EtSO4]) and Its Mixtures with Water," *Industrial & Engineering Chemistry Research*, Vol. 47, No. 23, 2008, pp. 9115–9126. https://doi.org/10.1021/ie800843u, URL https://doi.org/10.1021/ie800843u.

[11] Doherty, B., Zhong, X., Gathiaka, S., Li, B., and Acevedo, O., "Revisiting OPLS Force Field Parameters for Ionic Liquid Simulations," *Journal of Chemical Theory and Computation*, Vol. 13, No. 12, 2017, pp. 6131–6145. https://doi.org/10.1021/acs.jctc.7b00520, URL https://doi.org/10.1021/acs.jctc.7b00520, pMID: 29112809.

[12] Thompson, A. P., Plimpton, S. J., and Mattson, W., "General formulation of pressure and stress tensor for arbitrary many-body interaction potentials under periodic boundary conditions," *The Journal of Chemical Physics*, Vol. 131, No. 15, 2009, p. 154107. https://doi.org/10.1063/1.3245303, URL https://doi.org/10.1063/1.3245303.

[13] Martino, W., de la Mora, J. F., Yoshida, Y., Saito, G., and Wilkes, J., "Surface tension measurements of highly conducting ionic liquids," *Green Chem.*, Vol. 8, 2006, pp. 390–397. https://doi.org/10.1039/B515404A, URL http://dx.doi.org/10.1039/B515404A.

[14] Bhargava, B. L., and Balasubramanian, S., "Layering at an Ionic Liquid Vapor Interface: A Molecular Dynamics Simulation Study of [bmim][PF6]," *Journal of the American Chemical Society*, Vol. 128, No. 31, 2006, pp. 10073–10078. https://doi.org/10.1021/ja060035k, URL https://doi.org/10.1021/ja060035k, pMID: 16881635.

[15] Liu, H., and Cao, G., "Effectiveness of the Young-Laplace equation at nanoscale," *Scientific Reports*, Vol. 6, No. 1, 2016. https://doi.org/10.1038/srep23936, URL http://dx.doi.org/10.1038/srep23936.

[16] Romero-Sanz, I., Bocanegra, R., Fernandez de la Mora, J., and Gamero-Castaño, M., "Source of heavy molecular ions based on Taylor cones of ionic liquids operating in the pure ion evaporation regime," *Journal of Applied Physics*, Vol. 94, No. 5, 2003, pp. 3599–3605. https://doi.org/10.1063/1.1598281, URL https://doi.org/10.1063/1.1598281.

[17] Natisin, M. R., Zamora, H. L., McGehee, W. A., Arnold, N. I., Holley, Z. A., Holmes, M. R., and Eckhardt, D., "Fabrication and characterization of a fully conventionally machined, high-performance porous-media electrospray thruster," *Journal of Micromechanics and Microengineering*, Vol. 30, No. 11, 2020. https://doi.org/10.1088/1361-6439/abb8c3.

[18] Adduci, A. C., "Characterisation of a Multimode Propellant Operating in a Porous Glass Electrospray Thruster," Master's thesis, University of Illinois Urbana-Champaign, 2023.

[19] Williams, J. D., Gardner, M. M., Johnson, M. L., and Wilbur, P. J., "Xenon Sputter Yield Measurements for Ion Thruster Materials," *28th International Electric Propulsion Conference*, 2003, pp. IEPC–03–130.

[20] *Research Quartz Crystal Microbalance Instruction and Operation Manual*, Inficon Inc., 2014.

[21] Rao, A., Bhakyapaibul, T., Rovey, J., Levin, D. A., and Chew, H., *Plume-Material Interactions of Metallic Surfaces Bombarded by an [EMIM][BF$_4$] Electrospray Source*, American Institute of Aeronautics and Astronautics, Inc., 2022. https://doi.org/10.2514/6.2023-1407, URL https://arc.aiaa.org/doi/abs/10.2514/6.2023-1407.

[22] Prince, B. D., Tiruppathi, P., Bemish, R. J., Chiu, Y.-H., and Maginn, E. J., "Molecular Dynamics Simulations of 1-Ethyl-3-methylimidazolium Bis[(trifluoromethyl)sulfonyl]imide Clusters and Nanodrops," *The Journal of Physical Chemistry A*, Vol. 119, No. 2, 2015, p. 352–368. https://doi.org/10.1021/jp507073e, URL http://dx.doi.org/10.1021/jp507073e.

[23] Bruno, A., Schroeder, M., and Lozano, P. C., "Characterization of Electrospray Thrusters with HAN-Based Monopropellants for Multimode Propulsion Applications," *AIAA SCITECH 2022 Forum*, American Institute of Aeronautics and Astronautics, 2022. https://doi.org/10.2514/6.2022-2490, URL https://doi.org/10.2514/6.2022-2490.

[24] Oura, K., Katayama, M., Zotov, A. V., Lifshits, V. G., and Saranin, A. A., *Surface Science: An Introduction*, Springer Berlin Heidelberg, 2003. https://doi.org/10.1007/978-3-662-05179-5, URL https://doi.org/10.1007/978-3-662-05179-5.

[25] Bohdansky, J., "Universal Relation for the Sputtering Yield of Monatomic Solids At Normal Ion Incidence." *Nuclear Instruments and Methods in Physics Research, Section B: Beam Interactions with Materials and Atoms*, Vol. 230 (B2), No. 1-3, 1983, pp. 587–591.

[26] Yamamura, Y., and Tawara, H., "Energy dependence of ion-induced sputtering yields from monatomic solids at normal incidence," *Atomic Data and Nuclear Data Tables*, Vol. 62, No. 2, 1996, pp. 149–253. https://doi.org/10.1006/adnd.1996.0005.

[27] Ziegler, J. F., Ziegler, M., and Biersack, J., "SRIM – The stopping and range of ions in matter (2010)," *Nuclear Instruments and Methods in Physics Research Section B: Beam Interactions with Materials and Atoms*, Vol. 268, No. 11-12, 2010, pp. 1818–1823. https://doi.org/10.1016/j.nimb.2010.02.091, URL https://doi.org/10.1016/j.nimb.2010.02.091.

[28] Borrajo-Pelaez, R., and Gamero-Castaño, M., "The effect of the molecular mass on the sputtering by electrosprayed nanodroplets," *Applied Surface Science*, Vol. 344, 2015, pp. 163–170. https://doi.org/10.1016/j.apsusc.2015.03.077.

[29] Lozano, P., and Martínez-Sánchez, M., "Ionic liquid ion sources: Characterization of externally wetted emitters," *Journal of Colloid and Interface Science*, Vol. 282, No. 2, 2005, pp. 415–421. https://doi.org/10.1016/j.jcis.2004.08.132.

[30] Feder, R., Bundesmann, C., Neumann, H., and Rauschenbach, B., "Ion beam sputtering of Ag - Angular and energetic distributions of sputtered and scattered particles," *Nuclear Instruments and Methods in Physics Research, Section B: Beam Interactions with Materials and Atoms*, Vol. 316, 2013, pp. 198–204. https://doi.org/10.1016/j.nimb.2013.09.007, URL http://dx.doi.org/10.1016/j.nimb.2013.09.007.

[31] Kolasinski, R. D., Polk, J. E., Goebel, D., and Johnson, L. K., "Carbon sputtering yield measurements at grazing incidence," *Applied Surface Science*, Vol. 254, No. 8, 2008, pp. 2506–2515. https://doi.org/10.1016/j.apsusc.2007.09.082.

[32] Lozano, P. C., "Studies on the ion-droplet mixed regime in colloid thrusters," Ph.D. thesis, Massachusetts Institute of Technology, 2003. URL http://ssl.mit.edu/publications/theses/PhD-2003-Lozano-TovarPaulo.pdf.

[33] Cho, H., Moon, G.-W., Lee, S.-H., and Seo, H.-J., "Measurements of Outgassing from Satellites," *Environmental Testing for Space Programmes*, ESA Special Publication, Vol. 558, edited by K. Fletcher, 2004, pp. 445–452.